

## CMORPH: A Method that Produces Global Precipitation Estimates from Passive Microwave and Infrared Data at High Spatial and Temporal Resolution

ROBERT J. JOYCE

*Climate Prediction Center, NOAA/NCEP, Camp Springs, Maryland, and RS Information Systems, McLean, Virginia*

JOHN E. JANOWIAK

*Climate Prediction Center, NOAA/NCEP, Camp Springs, Maryland*

PHILLIP A. ARKIN

*Earth System Science Interdisciplinary Center, University of Maryland, College Park, College Park, Maryland*

PINGPING XIE

*Climate Prediction Center, NOAA/NCEP, Camp Springs, Maryland*

(Manuscript received 12 September 2003, in final form 21 January 2004)

### ABSTRACT

A new technique is presented in which half-hourly global precipitation estimates derived from passive microwave satellite scans are propagated by motion vectors derived from geostationary satellite infrared data. The Climate Prediction Center morphing method (CMORPH) uses motion vectors derived from half-hourly interval geostationary satellite IR imagery to propagate the relatively high quality precipitation estimates derived from passive microwave data. In addition, the shape and intensity of the precipitation features are modified (morphed) during the time between microwave sensor scans by performing a time-weighted linear interpolation. This process yields spatially and temporally complete microwave-derived precipitation analyses, independent of the infrared temperature field. CMORPH showed substantial improvements over both simple averaging of the microwave estimates and over techniques that blend microwave and infrared information but that derive estimates of precipitation from infrared data when passive microwave information is unavailable. In particular, CMORPH outperforms these blended techniques in terms of daily spatial correlation with a validating rain gauge analysis over Australia by an average of 0.14, 0.27, 0.26, 0.22, and 0.20 for April, May, June–August, September, and October 2003, respectively. CMORPH also yields higher equitable threat scores over Australia for the same periods by an average of 0.11, 0.14, 0.13, 0.14, and 0.13. Over the United States for June–August, September, and October 2003, spatial correlation was higher for CMORPH relative to the average of the same techniques by an average of 0.10, 0.13, and 0.13, respectively, and equitable threat scores were higher by an average of 0.06, 0.09, and 0.10, respectively.

### 1. Introduction

High time and space resolution estimates of precipitation are required for many important applications. Such datasets can provide useful information for disaster mitigation worldwide and can be used for initializing numerical models, driving land surface models, resolving the diurnal cycle of precipitation, and for validating model forecasts of precipitation. They can also be useful in diagnosing problems in numerical model forecasts. It is widely known that state-of-the-art global numerical models perform poorly in key areas of the globe, such

as over Indonesia, and there have been suggestions that the poor performance is related to improper modeling of the diurnal cycle (Yang and Slingo 2001). While global rain gauge data are routinely available around the world, that information is sparse in many important regions and is practically nonexistent over the oceans. Many gauge locations report only 6-h or even daily amounts. Remotely sensed estimates of precipitation from satellite with a temporal resolution of 3 h or less are required to provide the necessary information to assist the tasks mentioned above.

Infrared data are available globally nearly everywhere nearly all the time; however, IR channels measure cloud-top temperature, which does not always correlate well with rainfall. In many instances the cold cloud shield

---

*Corresponding author address:* Robert Joyce, RS Informations Systems, Inc., 1651 Old Meadow Road, McLean, VA 22102.  
E-mail: robert.joyce@noaa.gov

in a precipitating complex may be several times larger than the areal coverage of the actual precipitating region, sometimes with no rainfall directly under the coldest section. Cirrus cloud or decaying rainfall complexes with cold, but nonprecipitating, cloud can be easily mistaken for precipitating systems if IR data alone are used. Conversely, rainfall is not necessarily just associated with cold cloud. For example, rainfall in the eastern Pacific intertropical convergence zone (ITCZ) and orographically induced rainfall over northeastern Brazil often occurs from relatively low, warm clouds.

In contrast to the IR, relatively low frequency passive microwave (PMW) signals (10–37 GHz) sense the thermal emission of raindrops while higher frequencies (85 GHz and higher) sense the scattering of upwelling radiation from the earth to space due to ice particles in the rain layer and tops of convective systems. However, because of the technical challenges that have (to date) precluded the deployment of PMW sensors on geostationary platforms, these instruments are restricted to polar-orbiting platforms; thus, spatial and temporal sampling limitations from these observations are severe unless the data are averaged substantially over time. The left side of Fig. 1 shows typical global coverage percentage from the seven PMW satellites (at the time of writing) for consecutive half-hourly periods. The composite (Fig. 1, right) of the six half-hourly periods demonstrates that a large percentage of the earth is currently scanned by PMW sensors during a 3-h period. While the composite of the six half-hourly periods (Fig. 1, right) demonstrates that a large percentage of the earth is scanned by these PMW sensors during a 3-h period, the observation times vary by up to 3 h when compositing in this fashion. The following are 6-day averages of PMW satellite coverage, during each 3-h period, with both Northern and Southern Hemispheres combined in 10° latitude bands starting from the equator and ending at 60°N/S: 76.5%, 78.2%, 81.5%, 81.6%, 82.1%, and 84.2%.

The natural next step is to combine the data from these disparate sensors to take advantage of the strengths that each has to offer. A number of techniques have been developed in which the IR data are manipulated in a statistical fashion to mimic the behavior of PMW-derived precipitation estimates. Vincente (1994) combined PMW observations with IR data and radar over the Geostationary Operational Environmental Satellite (GOES) region. Miller et al. (2001) developed a technique in which PMW-derived precipitation estimates are regressed with collocated observations of IR brightness temperatures to generate precipitation estimates when and where PMW data are unavailable. Turk et al. (2003) developed a scheme to determine the IR brightness temperature threshold for precipitation by comparing the distribution of IR temperatures with collocated estimates of rainfall from PMW data, and the resulting relation-

ship is used to estimate rainfall from IR data in locations and instances where PMW data are not available. Huffman et al. (2003) developed a scheme in which PMW observations are used to calibrate the more frequently available IR data. In all of these techniques, precipitation estimates are calculated directly from IR data through an empirical relationship between the rain rate and cloud-top temperature, although regional calibrations can help to mitigate biases. As only one of several sources of error in this type of precipitation estimation, uncertainties exist in the quantitative accuracy of the cloud–precipitation relationship, especially over extratropical regions during nonsummer seasons where convective precipitation is not dominant (Arkin and Xie 1994).

An alternative method of combining these disparate data is proposed, one that uses precipitation estimates derived from low-orbiter-satellite PMW observations exclusively and whose features are transported via spatial propagation information obtained from geostationary satellite IR data during periods when instantaneous PMW data are not available at a location. Propagation vector matrices are produced by computing spatial lag correlations on successive images of geostationary satellite IR and then used to propagate the PMW-derived precipitation estimates in time and space when updated PMW data are unavailable. This process governs the movement of the precipitation features only. At a given location, the shape and intensity of the precipitation features in the intervening half-hour periods between PMW scans are determined by performing a time-weighted interpolation between PMW-derived estimates that have been propagated forward in time from the last available PMW observation and those that have been propagated backward in time from the next available PMW scan. This latter step, referred to as “morphing” of the features, produces spatially complete analyses of precipitation every half hour. This method is extremely flexible such that any precipitation estimates from any PMW satellite source can be incorporated. This technique is labeled “CMORPH,” short for the Climate Prediction Center (CPC) morphing method.

The data inputs are discussed in section 2. Details in which the PMW precipitation estimates are assembled, propagated, and morphed are in section 3. In section 4, validation results are presented, and conclusions along with a discussion of future plans are presented in section 5.

## 2. Instruments and data

### a. Infrared

The CPC operationally extracts geostationary satellite IR brightness temperature ( $T_b$ ) information (Janowiak et al. 2001) through the Man-computer Interactive Data Access System (McIDAS; Lazzara et al. 1999). CPC retrieves IR data from the satellites listed in Table 1 (at

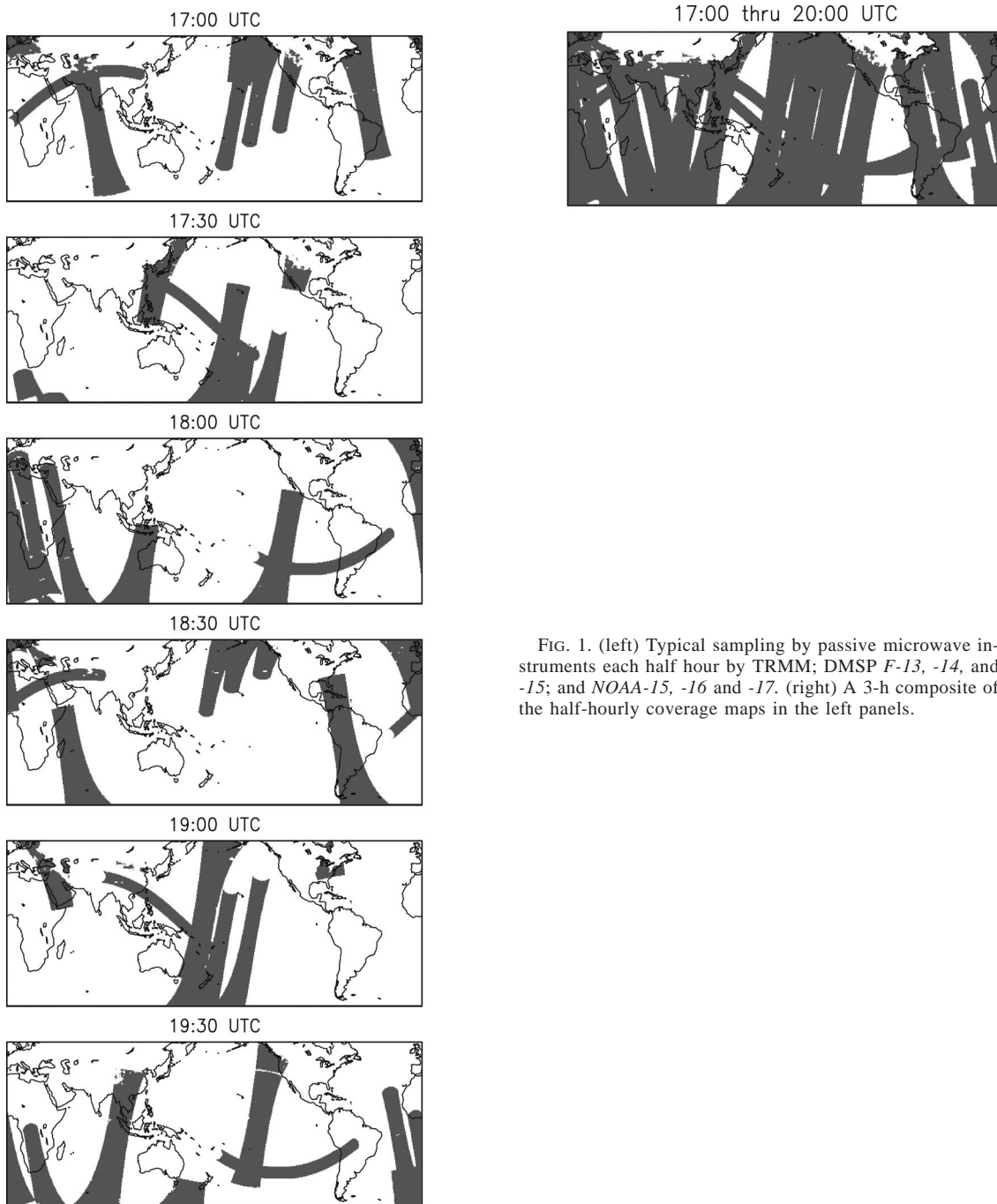


FIG. 1. (left) Typical sampling by passive microwave instruments each half hour by TRMM; DMSP *F-13*, *-14*, and *-15*; and NOAA-*15*, *-16* and *-17*. (right) A 3-h composite of the half-hourly coverage maps in the left panels.

the time of this writing). Full earth disk IR images are available from both the *Meteosat-5* and *Meteosat-7* satellites every 30 min, but only every 3 h from the GOES with Northern and Southern Hemispheric images for the intervening 30-min intervals. Full earth disk images are available from *Geostationary Meteorological Satellite-5 (GMS-5)* at hourly intervals. CPC maps each satellite IR image to a rectilinear grid at  $0.03635^\circ$  of latitude and longitude resolution ( $\sim 4$  km at the equator), parallax

corrects for geometric misnavigation of high cloud (Vicente et al. 1999), and corrects for cold limb effect of IR retrieval at large zenith angles (Joyce et al. 2001).

Figure 2 depicts the IR coverage (top) and image frequency (bottom) typically available daily from each of the operational geostationary satellites. Infrared sampling is good over the *Meteosat* and GOES domains. The *GMS-5* spacecraft generally provides full scans once per hour and currently only scans adequately in

TABLE 1. Characteristics of geostationary infrared data used in this study.

Satellite	Nadir location (at equator)	IR wavelength (microns)
<i>GOES-8</i>	75°W	10.7
<i>GOES-10</i>	135°W	10.7
<i>Meteosat-7</i>	0°	11.5
<i>Meteosat-5</i>	63°E	11.5
<i>GMS-5*</i>	140°E	11.0

\* At the time of writing, *GMS-5* was the operational western Pacific satellite; however, the technique described in this paper is applicable to any replacement satellite.

the region north of 10°S. The *GMS-5* scans less than 20 images per day in the Southern Hemisphere, with far fewer images in the far southern section.

### b. Passive microwave

The PMW-derived precipitation estimates that are presently used in CMORPH are generated from observations obtained from the NOAA polar-orbiting operational meteorological satellites, the U.S. Defense Meteorological Satellite Program (DMSP) satellites, and from the Tropical Rainfall Measuring Mission (TRMM; Simpson et al. 1988) satellite. The PMW instruments aboard these satellites are the Advanced Microwave Sounding Unit-B (AMSU-B), the Special Sensor Microwave Imager (SSM/I), and the TRMM Microwave Imager (TMI), respectively. The characteristics of these sensors are summarized in Table 2.

The TMI is a nine-channel radiometer that operates at five frequencies that are quite similar to the frequencies of the SSM/I instrument (Table 2). However, the TMI offers higher spatial resolution than SSM/I because of the relatively lower TRMM orbit, although the TRMM spacecraft orbit limits TMI's geographic coverage to 38°N to 38°S latitude. Surface rainfall derived from the TMI instrument is a product of the National Aeronautics and Space Administration's (NASA's) TRMM Science Data and Information System (TSDIS) 2A12 algorithm. This algorithm (Kummerow et al. 1996) relates the vertical profiles of liquid and ice to surface rain rates in a radiative model context, and rainfall estimates are derived over land and ocean. Recent modifications to this algorithm include matching of the convective/stratiform fraction satellite field of view precipitation with that of a cloud model (Hong et al. 1999). The current 2A12 Goddard profiling (GPROF) version 5 land rainfall estimation algorithm is a retrofit to the National Environmental Satellite, Data, and Information Service (NESDIS) SSM/I algorithm as described in Kummerow et al. (2001).

The SSM/I sensors aboard the DMSP platforms are operational on the *F-13*, *F-14*, and *F-15* satellites at the time of this writing. Precipitation estimates are used from the National Oceanic and Atmospheric Administration (NOAA)/NESDIS/Office of Research Applications SSM/I rainfall algorithm (Ferraro 1997), which utilizes the 85-GHz vertically polarized channel to relate the scattering of upwelling radiation by precipitation-sized ice particles within the rain layer and in the tops

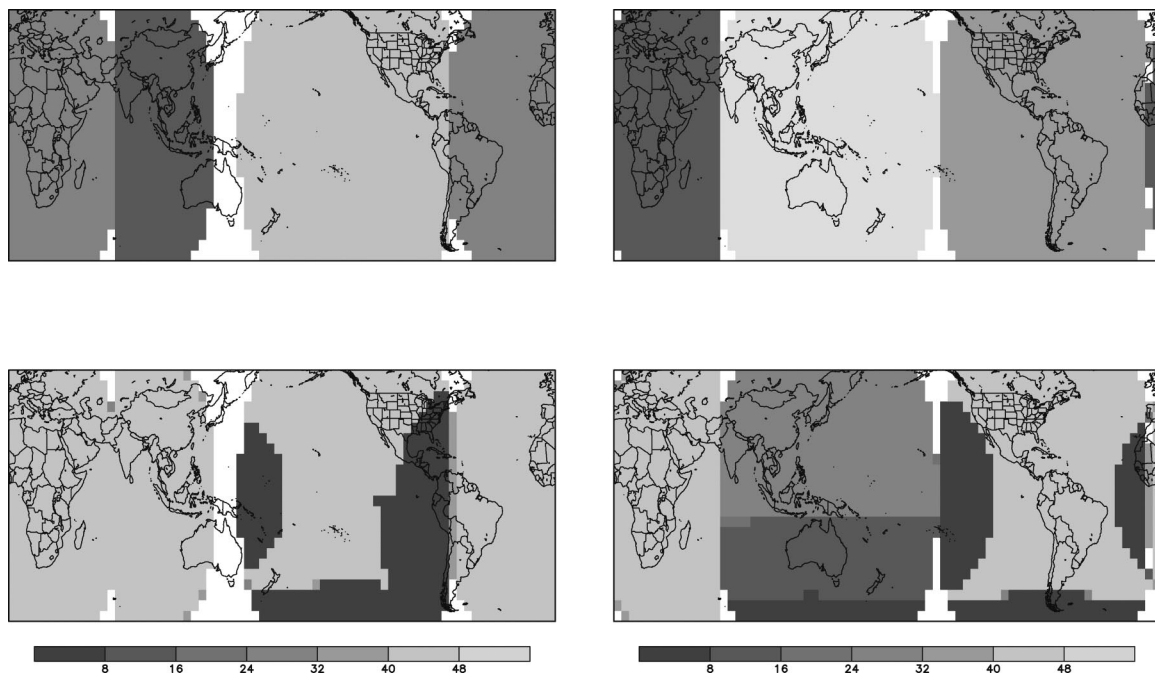


FIG. 2. (top) Templates of CPC geostationary IR satellite identification. (left) *GOES West*, *Meteosat-7*, and *Meteosat-5* east of 70°E. (right) *GMS-5*, *GOES East*, and *Meteosat-5* west of 70°E. (bottom) A typical number of available IR images over each satellite domain. This case is for 22 Dec 2002.

TABLE 2. Characteristics of PMW sensors and associated satellites used in this paper.

Sensor	Spatial resolution (footprint at $\sim 85$ GHz)	Observing time (ascending orbit)	Frequencies (GHz)	Altitude (km)
TMI	$4.6 \times 6.9$ km	Precessing orbit	10, 19, 21, 37, 85	402
SSM/I ( <i>F-13</i> )	$13 \times 15$ km	18:11	19, 22, 37, 85	830
SSM/I ( <i>F-14</i> )	$13 \times 15$ km	20:30	19, 22, 37, 85	830
SSM/I ( <i>F-15</i> )	$13 \times 15$ km	21:32	19, 22, 37, 85	830
AMSU-B ( <i>NOAA-15</i> )	$15 \times 15$ km*	18:58	89, 150, 183	830
AMSU-B ( <i>NOAA-16</i> )	$15 \times 15$ km*	13:57	89, 150, 183	830
AMSU-B ( <i>NOAA-17</i> )	$15 \times 15$ km*	22:08	89, 150, 183	830

\* Footprint for nadir view; limb footprint extends to 45-km diameter.

of convective clouds to surface precipitation. The scattering technique is applicable over land and ocean. A precipitation rate derived empirically from a relationship between ice amount in the rain layer and in the tops of convective clouds to actual surface rainfall is used to estimate precipitation amounts. The NESDIS ocean rainfall estimation technique is based upon the absorption of the upwelling radiation by rainwater and cloud water ("emission" technique) at 19 and 37 GHz. Error attributes of the algorithm are described by Li et al. (1998), Ferraro and Li (2002), and McCollum et al. (2002).

The AMSU-B instrument is currently operational aboard the *NOAA-15*, *NOAA-16*, and *NOAA-17* polar-orbiting satellites. The AMSU-B has five window channels, and its cross-track swath width (approximate 2200 km) contains 90 field of views (FOVs) per scan. The NESDIS AMSU-B rainfall algorithm (Ferraro et al. 2000; Zhao et al. 2001; Weng et al. 2003) performs a physical retrieval of ice water path (IWP) and particle size from the 89- and 150-GHz channels. Then a conversion from IWP to rain rate is made based on cloud data from the fifth-generation Pennsylvania State University–National Center for Atmospheric Research (NCAR) Mesoscale Model (MM5) and on comparisons with in situ data. The 183-GHz channel combined with surface temperature is used to screen out desert, and the 23-, 31-, and 89-GHz channels are used to screen out snow as described in Zhao and Weng (2002).

### c. Rainfall mapping

The CPC globally merged IR data analyses are available at half-hour intervals, so that time resolution was selected to produce spatially complete PMW precipitation analyses. The  $0.0727^\circ$  latitude and longitude (8 km at the equator) grid resolution used was determined by considering the spatial resolution of the various input data sources: 4-km (GOES IR), 5-km (Meteosat IR), and the greater-than-13-km resolution of the AMSU-B and SSM/I-derived precipitation estimates. Also, the grid must be small enough to represent the propagation of rainfall systems in half-hourly increments. Because the PMW rainfall estimates are coarser than the 8-km grid scale, the estimates are first mapped to the nearest

grid point on global ( $60^\circ\text{N}$ – $60^\circ\text{S}$ ) rectilinear grids at  $0.0727^\circ$  of latitude and longitude resolution, separately for each half hour and for each satellite. If two estimates from the same satellite sensor are mapped to the same grid point, the average rainfall is computed and used, although this situation only occurs for the higher-resolution TMI-based precipitation estimates. At locations within the grid where no rainfall estimates are available, an inverse distance squared weighting interpolation of the nearest rainfall estimates is performed to create a spatially complete field, but no extrapolation is performed beyond the last gridded estimate at the edge of a scan. Then for each half hour, satellite rainfall maps are combined by sensor type so that when the processes described above are completed, remotely sensed rainfall estimates for half-hourly periods for each sensor type (TMI, SSM/I, and AMSU-B) are saved to separate files. Precipitation fields that are composed of estimates with scan-swath time tags from 0 to 29 min after the hour are in separate files from those with time tags that range from 30 to 59 min after the hour. The half-hourly global IR data that are used to propagate the PMW precipitation estimates are averaged to 8-km resolution, to match exactly the grids that contain the PMW-estimated rainfall.

A precedence of sensor type had to be established to determine which estimate to use when a PMW-derived estimate from more than one sensor type is available at the same location for a given half-hourly period. Several estimates may be available for a given time and location because TRMM underflies all other low orbiters used in this study, and because some slight coverage overlap exists between the *NOAA-17* and DMSP *F-15* satellites in the half-hourly mapped rainfall files at the time of this writing. The order of precedence was established based on spatial resolution and the availability of both emission and scattering-based estimates over the oceans. The resulting order of precedence in regions of overlap is to use estimates from TMI first, then from SSM/I if no estimate from TMI is available, and finally AMSU-B. Each pixel in the half-hourly analyses is tagged with a satellite identification representing the orbiter used to produce the estimate.

### d. Surface snow and ice screening

Because snow and ice at the surface cannot be discriminated from frozen hydrometeors by any present-

day precipitation estimation algorithm, a snow-screening process is employed to locate areas of snow and ice over the earth's surface and to set nonzero rainfall estimates to values missing at locations where snow or ice are detected. The NESDIS Satellite Services Division (SSD) daily Interactive Multisensor Snow and Ice Mapping System (IMS) product is used as the snow-screening device. This product, which is available for the Northern Hemisphere only, has a spatial resolution of approximately  $1/10^\circ$  latitude/longitude. In order to use it as a screening tool, the product is mapped to the slightly higher-resolution PMW rainfall grid. This snow/ice-screening process is applied to the precipitation estimates that are generated from the various PMW sensors even though the NESDIS AMSU-B precipitation algorithm screens for snow and ice contamination.

*e. Normalization among the various microwave-derived precipitation estimates*

Rainfall estimates derived from the TMI and SSM/I instruments are in very good agreement (comparisons not shown), as is expected since the two sensors are quite similar in design, and the differences that do exist between them are attributable largely to the different retrieval footprint resolutions because they are flown at different altitudes. However, rainfall derived from the AMSU-B algorithm differs in many respects from SSM/I and TMI rainfall estimation techniques. Because the SSM/I and TMI instruments are equipped with channels that detect both emission and scattering signatures, the algorithms that are applied to these data generate precipitation estimates using similar channels. In contrast, the AMSU-B sensor only has high-frequency channels; thus, only precipitation that is detectable from a scattering signature can be estimated. Also, the relatively heavier AMSU-B oceanic rainfall has been determined to be 73% greater than Kwajalein gauge data rainfall, compared to only 12% greater for TMI V5 2A12 rainfall (Ji and Stocker 2003). Furthermore, the FOV of the cross-tracking AMSU-B varies considerably whereas the SSM/I is a conical scanner. Finally, at the time of this writing, the AMSU-B rainfall estimation algorithms have a  $20 \text{ mm h}^{-1}$  rain-rate maximum that is much less than the  $35 \text{ mm h}^{-1}$  maximum of the SSM/I land and ocean algorithms. Because these variations account for substantial differences in the nature of the distribution between the AMSU-B-derived oceanic rainfall and that from the SSM/I and TMI sensors, it was necessary to devise a normalization procedure.

A typical example of the sensor-type estimation differences is shown over the tropical Pacific in Fig. 3. Note the larger spatial coverage of rainfall area as determined by the AMSU-B (top) compared to TMI (middle). This quite different estimation nature can also be seen in histograms of temporally and spatially coincident 8-km rainfall estimates from both sensor types (Fig. 4). Over oceanic areas, the AMSU-B rainfall histogram

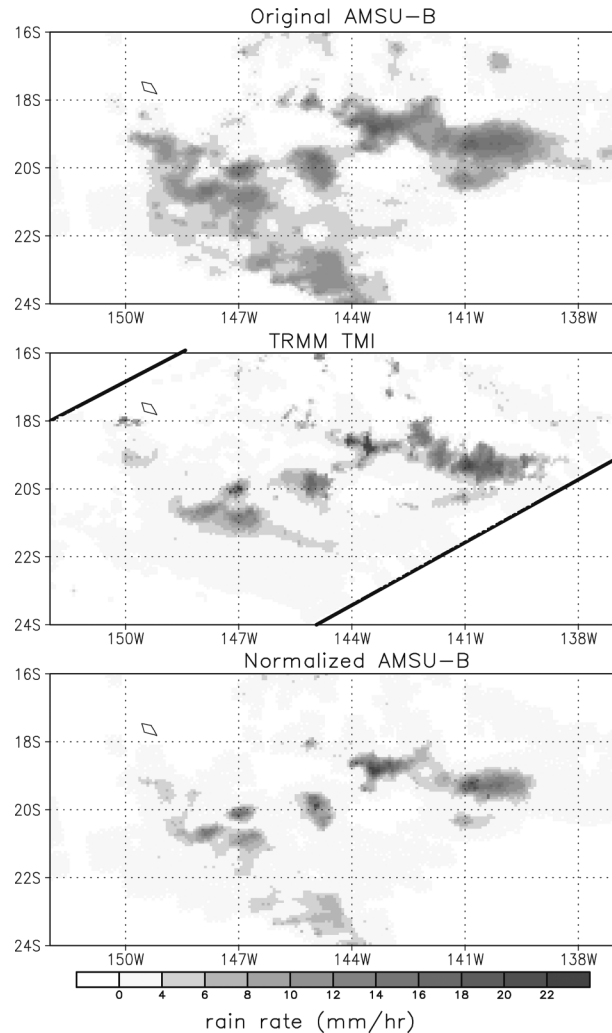


FIG. 3. Comparison among rainfall estimated from (top) NOAA-17 AMSU-B, (middle) TRMM TMI, and (bottom) NOAA-17 AMSU-B rainfall normalized to TMI and SSM/I rainfall for 2330 UTC 30 Nov 2002.

counts over the  $3\text{--}17 \text{ mm h}^{-1}$  range are far higher than the combined SSM/I and TMI rainfall distribution, although there are no AMSU-B derived estimates of rainfall above  $20 \text{ mm h}^{-1}$ , because of the maximum rainfall-rate limit in the AMSU-B precipitation algorithm. Conversely, the SSM/I and TMI counts far outnumber AMSU-B in the lightest rainfall categories over the oceans. Interestingly, the frequency of rainfall (i.e., the sum of all rainfall histogram counts) from AMSU-B and the SSM/I/TMI sensor group match very closely, both over land and ocean.

The SSM/I and TMI estimates were chosen as the normalization standard because of the finer spatial resolution and emission detection (ocean) of the SSM/I and TMI sensors. A revised AMSU-B rain-rate scale is determined dynamically by frequency matching 8-km mapped TMI and SSM/I precipitation estimates with

## Ocean surface

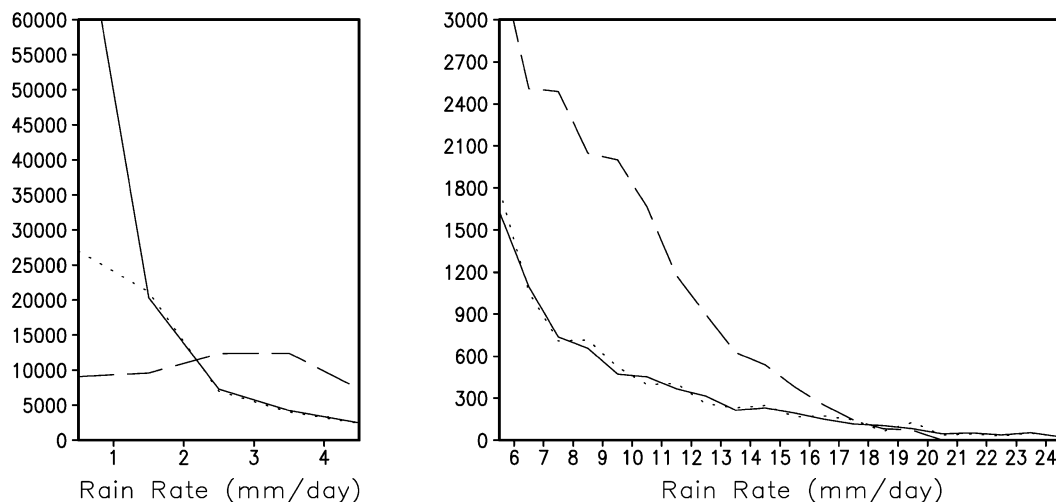


FIG. 4. Histograms of 8-km interpolated AMSU-B-derived oceanic precipitation collocated with rainfall derived from TMI and SSM/I instruments in  $1 \text{ mm h}^{-1}$  bins over the equator to  $30^\circ\text{N}$  zonal band: (left)  $0\text{--}5 \text{ mm day}^{-1}$  rainfall frequencies, and (right)  $5\text{--}25 \text{ mm day}^{-1}$  distribution. Solid line is for TMI-SSM/I, dashed line is AMSU-B, and dotted line is the normalized AMSU-B rainfall.

temporally and spatially coincident 8-km mapped AMSU-B estimates from the heaviest to lightest rain rates over the most recent 10-day period. The estimates used for matching are from intermediate, half-hourly, separate-sensor-type rainfall maps. The AMSU-B adjusted oceanic rainfall rates are calculated separately in  $10^\circ$  latitude bands from  $60^\circ\text{S}$  to  $60^\circ\text{N}$  by matching estimates in overlapping  $30^\circ$  latitude domains. Similar frequency rain-rate matching over land was also performed (not shown); however, since the distributions from the AMSU-B instrument reasonably matched those of TMI/SSM/I, normalization of AMSU-B land rainfall is not performed.

Examples of the amount of adjustment to AMSU-B-derived oceanic rain rates (Fig. 5) illustrate that there is a slight latitudinal dependency. Light to moderate AMSU-B rainfall is reduced substantially over the oceans, while the AMSU-B rain rates above  $16 \text{ mm h}^{-1}$  are adjusted sharply upward. The application of this adjustment information to the AMSU-B precipitation estimates results in patterns that resemble the collocated TMI estimates more closely (Fig. 3, bottom).

### 3. Methodology

#### a. Propagation vector derivation

The availability of IR data globally every half hour makes these data attractive to use as a means to propagate PMW-derived precipitation features, producing spatially and temporally complete global precipitation analyses. Since the IR data provide good measurements of cloud-top properties, IR data can be used to detect cloud systems and to determine their movement. In this

section, a method is described in which cloud system advection vectors (CSAVs) are derived.

Shenk and Kreins (1970) showed that it was possible to measure cloud motions from polar-orbiting satellites at locations where consecutive orbits overlap. Later a system known as WINDCO was developed to detect and estimate cloud motions from geostationary satellites (Smith and Phillips 1972). The first phase of the WINDCO program used an automated process that selects cloud targets that are either the coldest clouds or near regions where the IR gradient is strong (Herman 1992). Dills and Smith (1992) devised a specialized cloud relative motion tracking technique for cloud target recognition and velocity determination; however, this method uses 1-km *GOES-7* visible imagery and thus is usable during daytime only. Purdom and Dills (1994) state that researchers at the Cooperative Institute for Research in the Atmosphere (CIRA) have had success in deriving very accurate cloud motions, although the system required manual interaction.

The purpose for computing CSAVs for this project is to use them to propagate PMW-derived rainfall for each half hour of the day over the globe. This requires total automation and precludes the use of visible imagery. The method described below is similar to the WINDCO method in that the correlation between collocated IR imagery at two different time intervals are used to determine cloud motion. However, in order to reduce complexities, no cloud targeting is performed.

The direction and speed of cloud tops as detected by satellite IR may not always correlate well with the propagation of the lower precipitating layer of the system. Furthermore, wind direction changes and wind speed

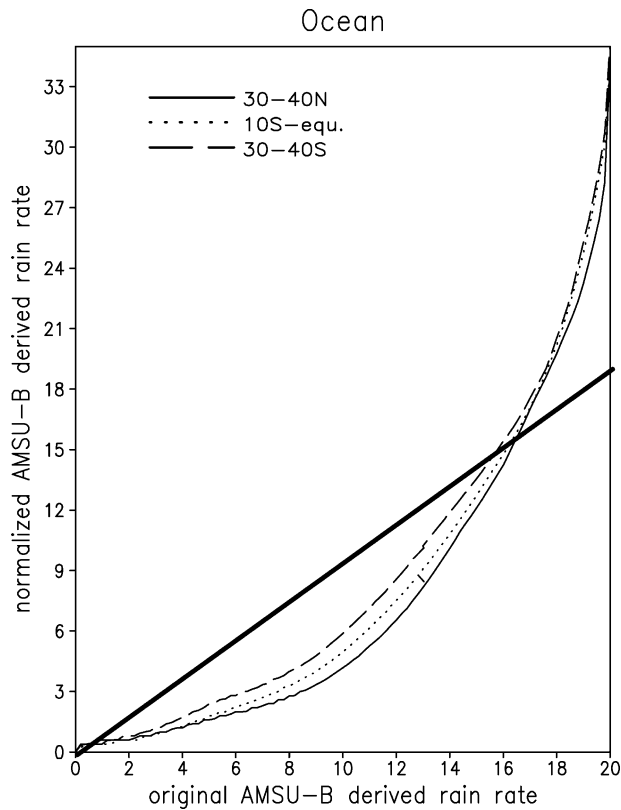


FIG. 5. Normalization adjustment of AMSU-B oceanic rainfall rates derived from previous 10 days of AMSU-B 8-km derived precipitation collocated with rainfall derived from TMI and SSM/I instruments. Normalizations shown are for 30°–40°N (solid line), 10°S–equator (dotted line), and 30°–40°S latitude (dashed line), for 11 Dec 2002;  $x$  axis is original, and  $y$  axis is adjusted AMSU-B-derived rain rate. The heavy straight line is the “1 to 1” line.

generally increases in magnitude with height from the earth’s surface. An optimal spatial lag correlation scale would be large enough to include the sharp contrast of the cloud shield edges with the earth’s surface, thus helping to focus on the motion of the entire cloud system rather than the smaller (and possibly higher and faster moving) cirrus or smaller plumes that may be imbedded within the entire cloud system complex. However, if the spatial resolution is too large, the resulting CSAV information may miss the variability of the steering currents that provide propagation of cloud system complexes. After various tests it was concluded for this work that spatially lagging overlapping 5° latitude/longitude IR regions centered at 2.5° latitude/longitude intervals provide a good measure of the movement of entire cloud systems while capturing the bulk of variations in the steering currents.

An iterative spatial lag correlation process is used to determine cloud system speed and direction as follows. At a given 5° latitude/longitude grid box that contains ~8 km pixel resolution IR data at time  $t=0$ , a spatial correlation is performed among the IR pixel brightness temperatures in that grid box with those in the same

domain but from the  $t+\frac{1}{2}$  h image. This process is repeated, but with each iteration the spatial domain of the  $t+\frac{1}{2}$  h grid box is shifted pixel by pixel in the zonal or meridional directions. The combination of lags that yields the highest correlation determines the CSAV. Both meridional and zonal vectors are assigned a value of zero for regions containing no cloud. Because only hourly data are available for *GMS-5*, the same procedure as described above is used except that the CSAV magnitudes are divided in two and are assumed to be the same for both half-hour periods within the hour.

Distinct meteorological patterns can be seen in both the zonal and meridional CSAV fields (Fig. 6, top and middle panels, respectively), with highest zonal values (positive) found in midlatitude jet streams and negative values found in the ITCZ. The maximum spatial lag correlation values generally exceed 0.9 for the GOES and Meteosat domains (Fig. 6c) but are somewhat weaker over the *GMS-5* domain because of the hourly sampling. Despite the lower correlations over the *GMS* domain (Fig. 6c), both the meridional and zonal CSAV fields (Figs. 6a,b) are contiguous at neighboring satellite boundaries (178.5°E, 101.5°E north of 10°S, and 135.0°E south of 10°S) where sampling is good.

A primary domain is defined for each satellite, demarcated by the midpoints between the nadir positions of primary and neighboring satellites. Within each domain, CSAVs are derived solely from the primary satellite IR unless the daily image count falls below half of the overlapping neighboring satellite daily image count; in this case, information from the neighboring satellite is used instead. When an image is missing for a particular half hour, vectors are determined by a linear temporal interpolation between the nearest past and future half-hourly vectors, weighted by the temporal distance from the missing time. A spatial interpolation of CSAV fields is performed only in very small regions where missing vectors remain. Over the GOES and *GMS* domains south of 50°S, where IR data are very sparse, no spatial or temporal interpolation is performed, and vectors in those regions are set to zero.

Early versions of CMORPH used CSAVs directly to propagate PMW-derived precipitation. However, it was soon determined that the west to east and south to north advection rates were too fast in the North Hemisphere midlatitudes (Fig. 7). To correct this, a speed adjustment procedure was developed by first computing rainfall advection vectors by spatially lagging hourly U.S. Next-Generation Weather Radar (NEXRAD) stage II (Klazura and Imy 1993) radar rainfall (mapped to the same 8-km grid) in the exact same dimensions and manner CSAVs are computed from IR. The half-hourly CSAV data were then combined to hourly to match the radar rainfall vectors. The frequency distribution of hourly CSAV and radar rainfall advection rates indicated that north to south rates are quite similar but that west to east CSAV speeds were about twice as fast compared

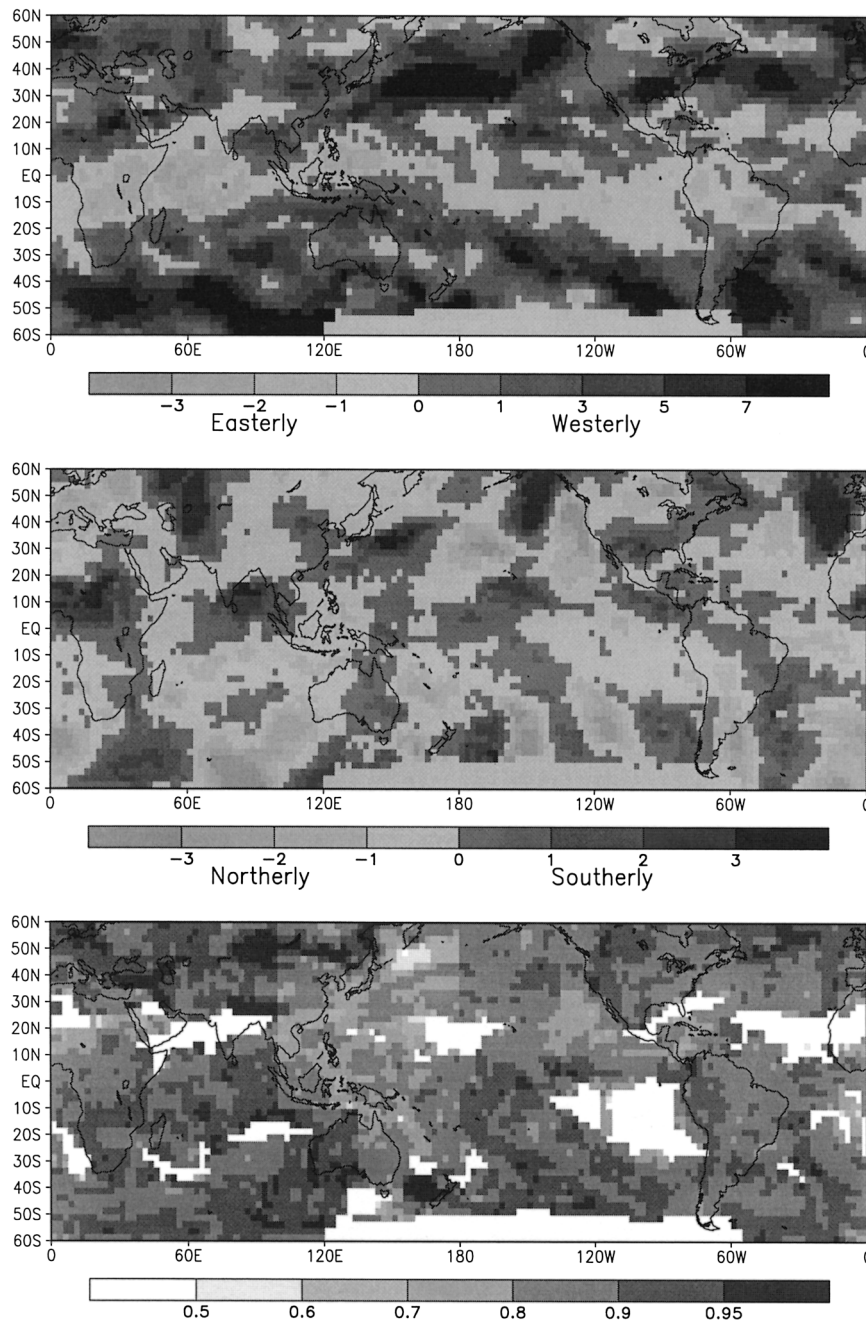


FIG. 6. (top) IR-derived zonal half-hourly cloud system vectors, (middle) meridional, and (bottom) the maximum spatial lag correlations for 22 Dec 2002. Positive zonal (meridional) propagation values are westerly (southerly) in units of 0.0727 lat/lon increments per 30 min.

to the radar-derived vectors, and south to north rates were 3–4 times faster (Fig. 7). These systematic differences are consistent with several case studies that show the tendency of IR features to quickly stream to the northeast on the east side of long-wave troughs, with the actual rainfall also moving in this direction but at a slower rate. The incorporation of this adjustment procedure into the CMORPH processing has resulted in

improved propagation of precipitation features. For consistency with the Northern Hemisphere, the meridional adjustment is applied to vectors of the opposite sign in the Southern Hemisphere in order to reduce the same long-wave-trough effect. Further tests have shown that there is scant seasonal dependence in the relationship between the IR-derived and radar-derived advection vectors.

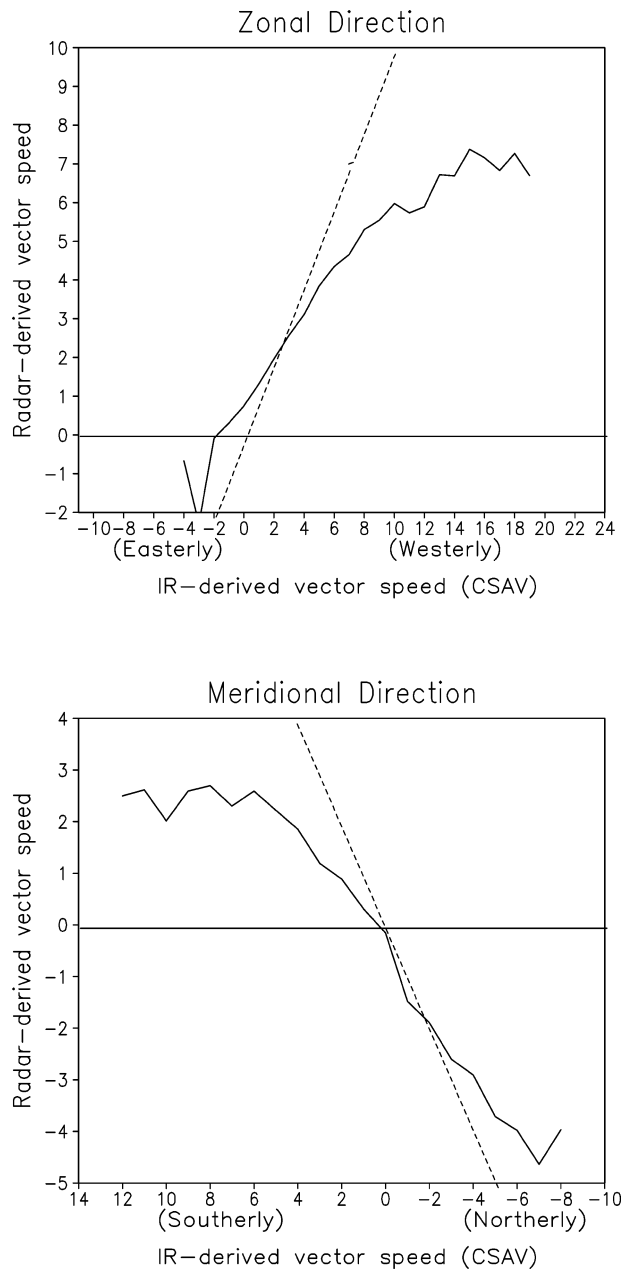


FIG. 7. Hourly precipitation advection vector equivalence in  $0.0727$  lat/lon increments (y axis) relative to hourly cloud system advection vectors (x axis) over the United States during 15 May–15 June 2003. (top) Zonal vector equivalence, and (bottom) meridional Vector equivalence.

### b. Microwave rainfall propagation and morphing

The PMW rainfall propagation process begins by spatially propagating initial fields of 8-km half-hourly instantaneous PMW analysis estimates ( $t+0$  h) forward in time, by the discrete distance of the corresponding zonal and meridional vectors. Two auxiliary fields that are maintained along with each precipitation estimate are 1) time stamp ( $t=0$  for instantaneous), in which the

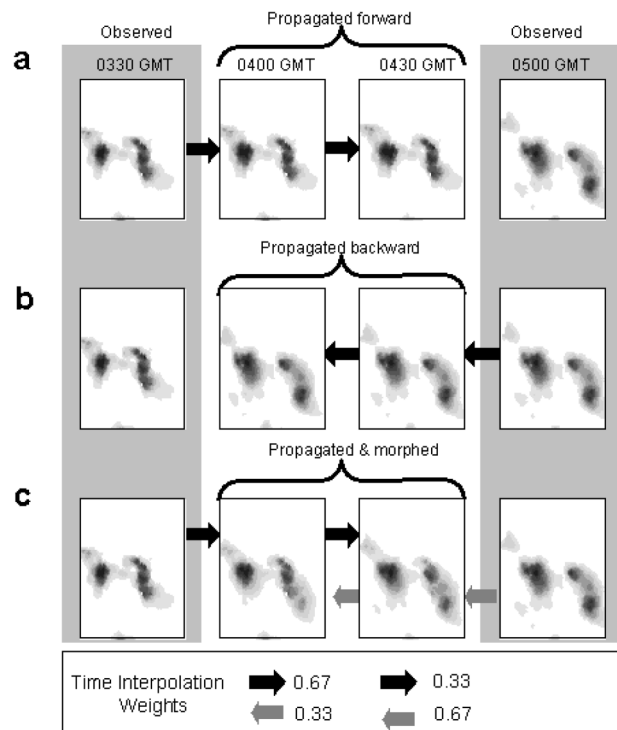


FIG. 8. Depiction of the propagation and morphing process for a region in the South Pacific. The analyses at 0330 and 0500 UTC are actual passive microwave estimates, i.e., no propagation or morphing has been applied to these data. The 0400 and 0430 UTC are (a) propagated forward in time, (b) propagated backward in time, and (c) propagated and morphed.

units represent the time, in half-hourly increments, since the scan of the PMW satellite overpass used to define that pixel and 2) satellite identification. All PMW satellite pixels (including those with zero precipitation) within each  $2.5^\circ$  latitude/longitude region are propagated in the same direction and distance to produce the analysis for the next half hour ( $t+0.5$  h). If a PMW rainfall feature is on the border between two of the  $2.5^\circ$  latitude/longitude regions, the rainfall field is propagated evenly if the vector pairs from both regions match exactly. If two pixels from different regions are propagated to the same pixel location by convergence, an average of the two values is computed. If a data gap in the rainfall field is created by divergence, a bilinear interpolation of the rainfall features across the gap is computed. Finally, if a PMW-derived precipitation estimate from a new scan at  $t+0.5$  h is available at a particular pixel location, then that estimate overwrites the propagated estimate and the associated time stamp for that pixel is set to a value of zero. Otherwise, the time stamp is incremented by a value of 1. This entire process is repeated each half hour.

The propagation process is illustrated graphically in Fig. 8. An initial 0330 GMT time analysis of instantaneous PMW rainfall ( $t=0$  h) consisting of two clusters over a region in the South Pacific (Fig. 8a, leftmost

column) is propagated forward to produce analyses at  $t+0.5$  and  $t+1$  h (Fig. 8a) using the IR-derived propagation vectors. This analysis is actually propagated one more time step to  $t+1.5$  h (not shown), but in this case all values are overwritten by precipitation estimates from an updated PMW scan (Fig. 8a, rightmost column) that became available at the  $t+1.5$  h time step (0500 UTC). The continuity of the propagated rainfall clusters in the  $t+0.5$  and  $t+1.0$  h fields can be appreciated by comparing them with the updated PMW analysis (Fig. 8a, rightmost column), although in this case, the propagation rate appears to be slightly slow. Note that the shape and intensity of the features have not changed in the propagated plots, which is an aspect that will be discussed shortly.

In addition to propagating rainfall estimates forward in time, a completely separate process is invoked in which instantaneous rainfall analyses are spatially propagated backward in time using the same propagation vectors used in the forward propagation, except for reversing the sign of those vectors. The results are stored separately from those computed in the forward propagation process. Thus for the above example, the  $t=1.5$  h updated observed PMW precipitation (Fig. 8b, rightmost column) is propagated backward to the  $t=0$  h time frame (Fig. 8b, leftmost column). When all propagated fields have been computed, the  $t=0$  h analysis that contains observed data overwrites the propagated estimates for that time stamp. Because of temporal sampling considerations imposed by the orbital nature of the spacecraft, the backward propagation procedure must begin at least 5 h beyond the initial analysis time ( $t=0$ ) in order to have a nearly globally complete field of backward-propagated rainfall estimates. This constraint delays the operational availability of CMORPH by 5 h previous to the most current half hour of combined PMW rainfall input analyses. However, by propagating the rainfall analyses temporally in both directions, the propagation speed and direction is improved over doing this in a single direction (in time) only.

To this point, only the propagation of PMW-derived rainfall patterns, when and where PMW data are not available, has been shown. However, a simple propagation of the features themselves will not change the character of those features but will merely translate them to new positions. Changes in the intensity and shape of the rainfall features are accomplished by inversely weighting both forward- and backward-propagated rainfall by the respective temporal distance from the initial and updated *observed* analyses. This process is referred to here as “morphing” and is represented graphically in Fig. 8c. At each pixel location, the process by which the 0400 UTC ( $t+\frac{1}{2}$  h) estimate is produced (Fig. 8c, second column from the left) involves creating a weighted mean as follows:

$$\text{Morphed Value}_{(t+1/2h)} = 0.67 \times P_{\text{forward}(t+1/2h)} + 0.33 \times P_{\text{backward}(t+1/2h)}, \quad (1)$$

where  $P_{\text{forward}}$  is the PMW precipitation estimate forward propagated from the initial analysis (0330 UTC), and  $P_{\text{backward}}$  is the PMW precipitation estimate backward propagated from the updated analysis (0500 UTC).

Similarly, the CMORPH value for the 0430 UTC analysis is computed as follows:

$$\text{Morphed Value}_{(t+1h)} = 0.33 \times P_{\text{forward}(t+1h)} + 0.67 \times P_{\text{backward}(t+1h)}. \quad (2)$$

Each CMORPH estimate’s associated time stamp and satellite identification are extracted from the propagated estimate (forward or backward) with the smallest time stamp. For CMORPH derived from instantaneous PMW information, time stamp = 0.

#### 4. Validation

The CMORPH estimates were validated using high quality rain gauge data over the United States and Australia and radar data over the United States. Thus, even though less than a year of CMORPH analyses were available at the time of this writing, we can show comparisons for both a warm and cold season. The U.S. rain gauge information that was used in this validation exercise is the Climate Prediction Center Realtime Daily Gauge Analysis (Higgins et al. 2000), which is composed of over 7000 stations, has undergone quality control including “buddy checks,” and has been objectively analyzed (Cressman 1959) to a  $0.25^\circ$  latitude/longitude grid. The Australian rain gauge analyses were obtained from the Bureau of Meteorology (BOM), where the original gauge data were objectively analyzed using a multipass, inverse-weighting scheme in which the observations were gridded to a  $0.25^\circ$  latitude/longitude grid (Weymouth et al. 1999). The “stage II” hourly radar composites over the United States were also used to validate the CMORPH estimates. These radar analyses are available hourly and are composites of all available radars over the United States, but with no intercalibration nor calibration to or integration with rain gauge data. However, the gauge data are used to perform a mean-bias adjustment on the radar estimates (R. Kulligowski 2002, personal communication). For the validation results that follow, all datasets were gridded to a common  $0.25^\circ$  lat/lon daily grid. Note that several of the statistics that appear in the text and figures were computed from  $2 \times 2$  contingency tables in which the categories are  $<1$  and  $\geq 1$  mm day $^{-1}$ , and those statistics were computed as described in Wilks (1995).

##### a. United States

Comparisons are presented over the United States for the 15 June through 15 November 2003 period only because the estimates from other blended PMW–IR estimated rainfall estimation techniques were available for that period. Time series of U.S. rain gauge analyses

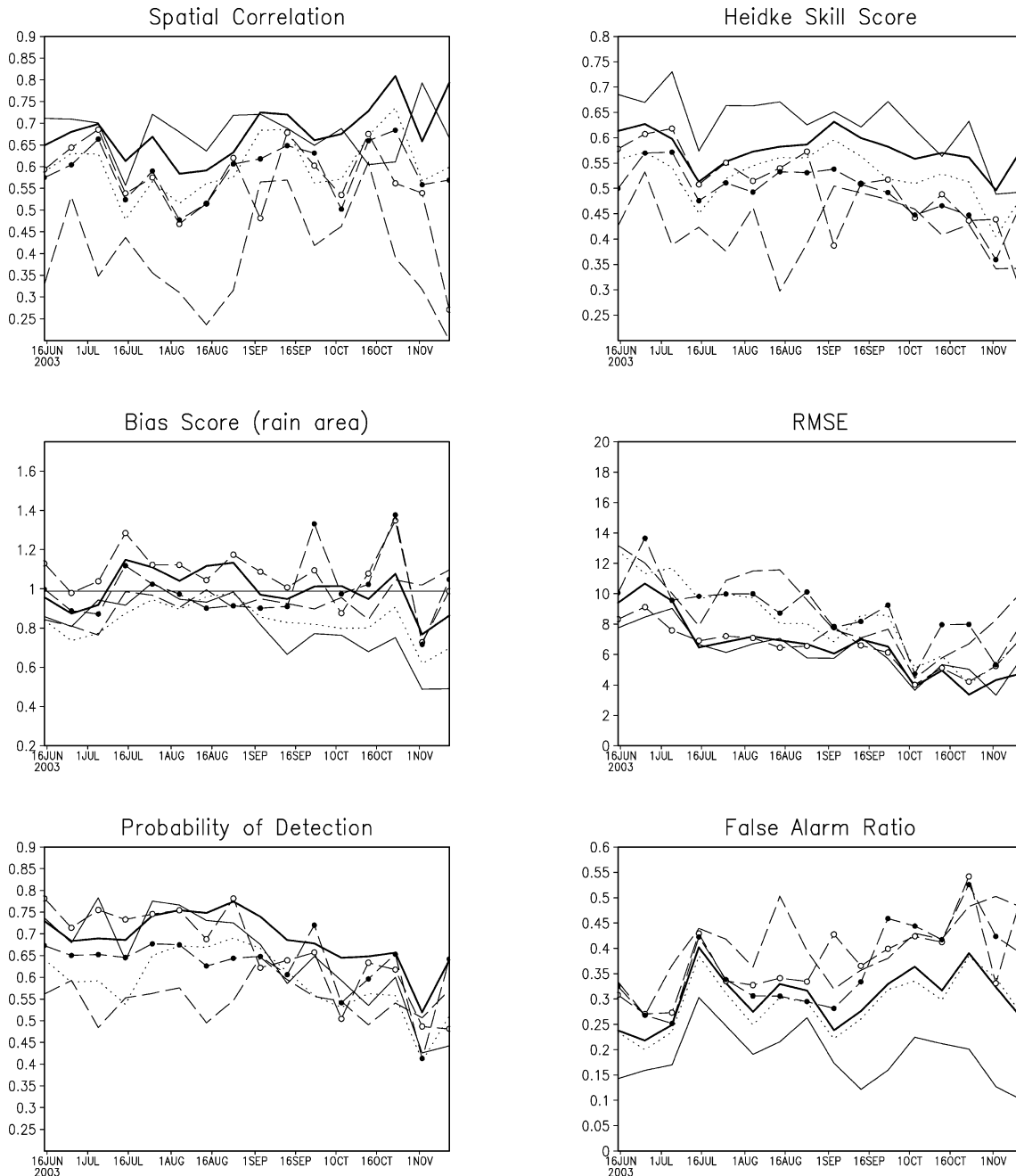


FIG. 9. Time series of selected statistics of U.S. rainfall estimation validation during the 15 Jun–15 Nov 2003 period, with statistics generated every 10 days using daily estimates. Solid thick line is CMORPH, solid thin line is radar rainfall, dotted line is MWCOMB, and remaining lines are other blended microwave–IR rainfall estimation techniques.

comparisons with six indirect measurements of rainfall, statistics generated every 10 days using daily estimates, are illustrated in Fig. 9. The indirect measurements are radar, CMORPH, three blended microwave–IR rainfall estimation techniques that use IR data to derive precipitation when PMW data are unavailable, and MWCOMB, which is a daily average of all available microwave-derived precipitation estimates but without

any propagation or morphing of the features. Each dataset was interpolated to match the validating gauge analysis resolution, and if a data value at a grid location was missing for one of the six indirect estimates, it was set to missing in all of them to ensure temporal and spatial matching among the various data.

Radar and CMORPH compare best with the gauge analyses over the United States in most of the statistics,

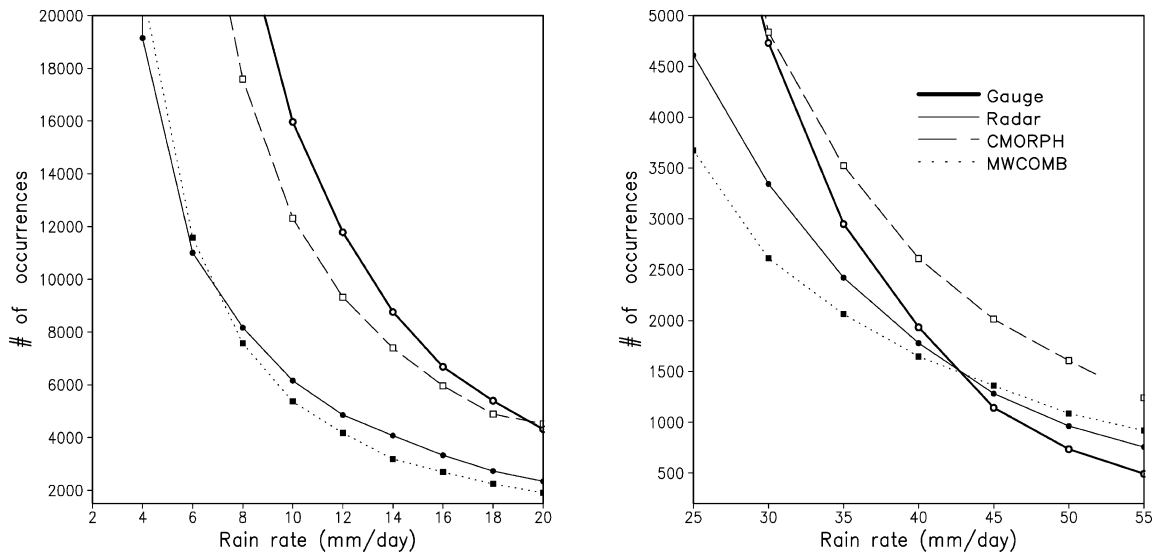


FIG. 10. Histogram of daily rain rates over the United States during Apr–May 2003 ( $\text{mm day}^{-1}$ ). Data source is identified in the legend in the plot on the right. Numbers on y axis are the number of rain-rate occurrences. (left) Histogram rain rates from 0 to 20  $\text{mm day}^{-1}$  in 2  $\text{mm day}^{-1}$  increments, and (right) histogram rain rates from 20 to 55  $\text{mm day}^{-1}$  in 5  $\text{mm day}^{-1}$  increments. Numbers on the x axis represent histogram rain-rate boundaries. Note scale change on y axis between the plots.

with radar outperforming CMORPH in skill. However, the correlation and root-mean-square error values are quite similar for both, while CMORPH has better bias characteristics than radar over the latter half of the period and higher probability of detection (POD) scores during the entire period. The underestimation of rain area by radar occurs primarily in the western United States because of blockage by terrain. Radar is superior to all of the other indirect precipitation estimates in terms of false alarm ratio (FAR). CMORPH outperforms the three other IR/PMW–IR blended methods in almost every validation statistic, except for bias, for the entire 6-month validation period, especially in the late summer to fall period. In particular, in daily validation statistics averaged for the period June–August and months September and October 2003, CMORPH correlation values of 0.65, 0.74, and 0.67 and equitable threat scores of 0.42, 0.43, and 0.37, respectively, outperform the same three PMW–IR blended techniques in correlation by an average of 0.10, 0.13, and 0.13 and equitable threat score by an average of 0.06, 0.09, and 0.10, respectively. Perhaps more importantly, CMORPH compares more favorably than MWCOMB with the gauge analyses in all statistics (except FAR). The difference in correlation with the rain gauge analyses between CMORPH and MWCOMB is statistically significant at the 1% level. This result is important because it illustrates that propagation and morphing have positive impacts on the estimates.

The distribution of daily rain rates among the rain gauge, radar, CMORPH, and MWCOMB analyses over the United States during April through May 2003 is depicted in histogram form in Fig. 10. At rainfall intensities between 2 and 25  $\text{mm day}^{-1}$ , all indirect mea-

surements of precipitation detect less area with rainfall compared to the gauge analyses. At rain rates higher than 25  $\text{mm day}^{-1}$ , however, all three indirect estimates have more rainfall area compared to the gauges. Note that CMORPH agrees best with the gauge distribution of rainfall rates for the 4–45  $\text{mm day}^{-1}$  range, followed by radar, then MWCOMB. At rain rates above 45  $\text{mm day}^{-1}$ , all three indirect measurement share very similar distributions. However, it is well known that objective analyses of rainfall tend to suppress high rainfall amounts because of smoothing, especially in analyses that use Cressman (1959) approaches, so the comparison at high rain rates should be viewed judiciously.

*b. Australia*

Displayed in Fig. 11 is a comparison during the December 2002 through May 2003 period of statistics generated every 10 days using daily estimates of CMORPH, MWCOMB, and GOES precipitation index (GPI; Arkin and Meisner 1987), which is an estimate based on infrared data, with Australian rain gauge analyses. The CMORPH estimates compare best with the gauge analyses overall during this period and consistently outperforms MWCOMB. The performance of all of these indirect estimates decreases after March when the Australian rainy season begins to wane. The good performance of the GPI is noteworthy during December–March, which is the main part of the rainy season over Australia. The low Rmse in the GPI estimates is most likely because the GPI technique is constrained to a maximum rainfall amount of 3  $\text{mm h}^{-1}$ . However, the skill, variability, bias, and detection capabilities of the GPI are extremely similar to CMORPH and sometimes

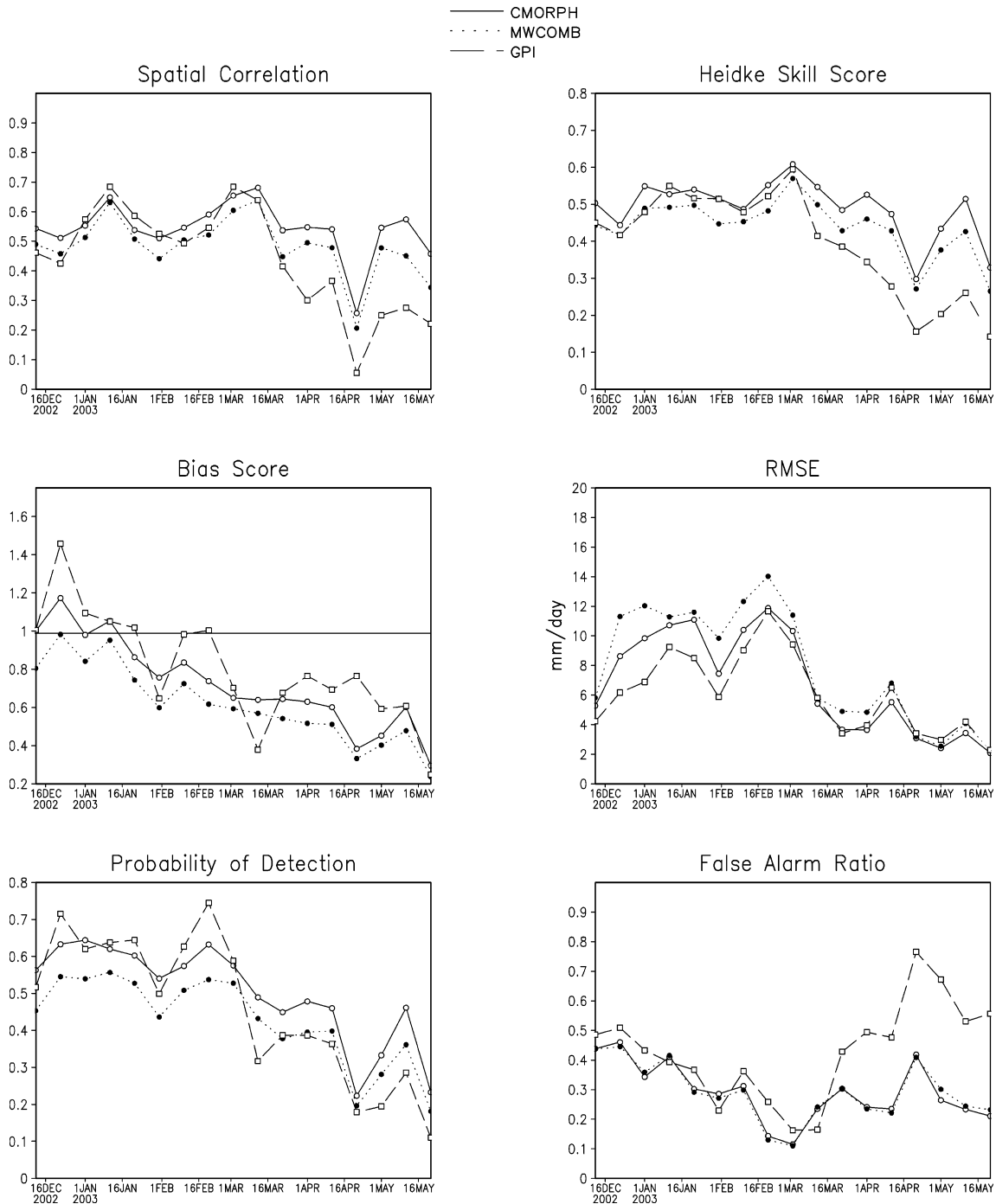


FIG. 11. Time series of selected statistics of Australian rainfall estimation validation during the Dec 2002 through May 2003 period, with statistics generated every 10 days using daily estimates.

slightly better during the rainy season over Australia. According to the BOM statistical validation summaries, CMORPH correlation values of 0.51, 0.57, 0.64, 0.60, and 0.70, generated for months April, May, the June–August period, and months September, October 2003, respectively, using daily estimates over Australia, out-

performs the three IR–PMW blended methods (used in U.S. comparison) by an average of 0.14, 0.27, 0.26, 0.22, and 0.20. Also from the BOM summaries, CMORPH daily equitable threat score averages of 0.30, 0.28, 0.26, 0.33, and 0.36 for the same respective periods outperform the same three leading PMW–IR

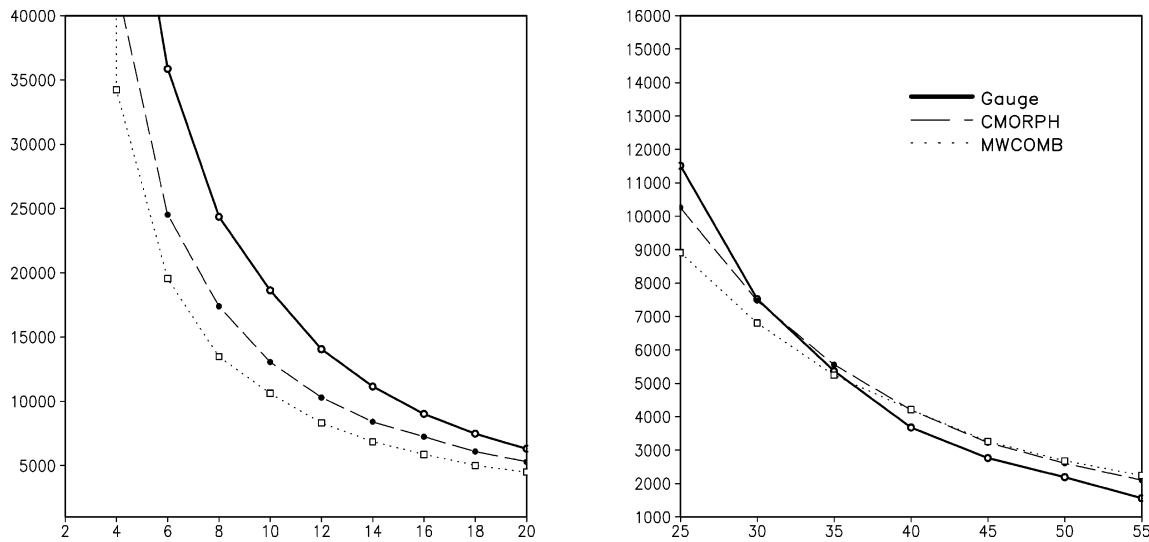


FIG. 12. Histogram of rain rates over Australia during Dec 2002–May 2003 in  $\text{mm day}^{-1}$  units. Data source is identified in the legend in the plot on the right. Numbers on y axis are the number of rain-rate occurrences. (left) Histogram rain rates from 0 to 20  $\text{mm day}^{-1}$  in 2  $\text{mm day}^{-1}$  increments, and (right) histogram rain rates from 20 to 55  $\text{mm day}^{-1}$  in 5  $\text{mm day}^{-1}$  increments. Numbers on the x axis represent histogram rain-rate boundaries. Note scale change on y axis between the plots.

blended techniques by an average of 0.11, 0.14, 0.13, 0.14, and 0.13, respectively.

The daily rain-rate distribution for rain rates  $<20 \text{ mm day}^{-1}$  between CMORPH and the rain gauge data are quite similar over Australia and the United States (Figs. 12 and 10, respectively) while the MWCOMB distribution differs substantially from the gauge data. For rain rates  $>20 \text{ mm day}^{-1}$ , the distributions are all very similar over Australia in contrast to large differences over the United States. The distribution differences for the higher rain rates may be associated with the fact that the rainfall over Australia is during the warm season and is thus primarily convective in nature while over the United States the rainfall occurred during spring and therefore contains a mixture of convective and stratiform precipitation.

## 5. Summary, conclusions, and future work

Half-hourly analyses of CMORPH at a grid resolution of 8 km (at the equator) have been produced operationally since 22 November 2002. Some modifications have been made to the scheme since the processing became operational, most importantly the implementation of an improved snow-screening process. Validation of the CMORPH analyses indicate that the method is consistently better than blended IR–PMW rainfall estimation techniques that use IR-derived estimates of rainfall when PMW data are not available. Furthermore, CMORPH estimates perform better than mere composites of PMW precipitation analyses and sometimes perform better than radar. This indicates that the propagation and morphing procedures have positive impacts compared to simply compositing all available PMW information.

There are several issues that CPC will continue to investigate. One is the development and implementation of a more accurate method to screen out anomalously high PMW rainfall related to ice or snow cover. Also, at present, a simple linear time interpolation process morphs the precipitation features. Although this process appears to work well, use of a Kalman filtering technique, widely used to morph imagery, may be able to improve the analyses. The possibility of extending the CMORPH analyses back in time—perhaps back to the early to mid-1990s—will be investigated. The limiting factor is the availability of sufficiently dense PMW coverage and pixel resolution IR data.

A potential shortcoming of the CMORPH method is that when precipitation forms and dissipates over a region between overpasses by PMW instrumentation it will not be detected. CPC plans to investigate ways to use the IR data to provide estimates for these situations. Another way to alleviate this problem is to ingest more PMW information, and future CMORPH plans include incorporating Advanced Microwave Scanning Radiometer for the Earth Observing System (AMSR-E) instrument precipitation estimates when they become available. Increased sampling by PMW instruments will help CMORPH considerably more than techniques that use IR to make precipitation estimates in the absence of PMW information. Although all techniques will benefit from increased availability of PMW information from a purely sampling perspective, the methods that estimate precipitation from IR can expect only marginal additional improvement in the statistical relationship between IR-derived and PMW-derived precipitation estimates because of more PMW data. Meanwhile, as demonstrated in Fig. 13, CMORPH stands to gain substan-

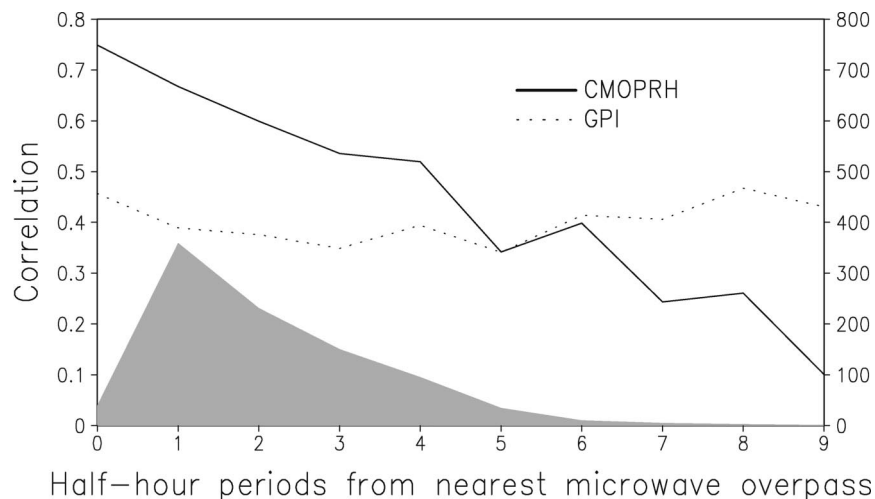


FIG. 13. Correlation between radar and CMORPH (solid line) as a function of half-hour periods from nearest future or past microwave satellite overpass ( $x$  axis) for the period Apr–May 2003. For reference, the dotted line represents the correlation between radar and GPI over the same locations and times that were used in the radar–CMORPH correlation calculations. Shaded plot shows the number of pairs in the correlations; the scale for that plot is on the right ( $y$  axis label in 1000s).

tially with the availability of more passive PMW information. This figure shows the correlation of hourly, CMORPH precipitation estimates with radar rainfall over a 2-month period (April–May 2003) as a function of time from the nearest future or past PMW overpass. Note that the correlation with radar jumps from near a value of 0.40 when the most recent information is 2.5 h from PMW overpass (time step 5 on the  $x$  axis) to about 0.55 when PMW information is only 1.5 h from scan time, which represents a 90% improvement in explained variance.

The information in Fig. 13 also provides insight concerning conditions when IR-based estimates would be useful additions to the CMORPH technique. Note that correlation of GPI with radar rainfall exceeds that of CMORPH and radar rainfall after time step 6, which means that for this spring case study over the United States, GPI is a better estimate than CMORPH when the nearest past or future PMW pass is more than 3 h away. CPC will examine the relative performance of CMORPH and IR-based estimates to available validation and use that information to devise a strategy on the use of IR-based rainfall in conjunction with the propagation and morphing aspects of CMORPH.

Because CMORPH is flexible and can incorporate precipitation information from any algorithm based on information from any instrument, the technique is highly complementary to the proposed Global Precipitation Mission (GPM). This mission is planned to begin in 2008 as a follow-on to the highly successful TRMM project and may provide 3-hourly sampling from PMW sensors. CPC looks forward to incorporating precipitation products from GPM into the CMORPH scheme. And while GPM may provide sampling from PMW ra-

diometers every 3 h, CMORPH can add considerable value to GPM precipitation products by melding them with IR data to increase their temporal resolution to 30 min.

*Acknowledgments.* The authors wish to acknowledge Vern Kousky and George Huffman for their useful suggestions and Chet Schmitt, S. K. Yang, and the four peer reviewers for their constructive and helpful comments and suggestions. This work was funded partially by the NASA TRMM project.

#### REFERENCES

- Arkin, P. A., and B. N. Meisner, 1987: The relationship between large-scale convective rainfall and cold cloud over the Western Hemisphere during 1982–1984. *Mon. Wea. Rev.*, **115**, 51–74.
- , and P. Xie, 1994: The Global Precipitation Climatology Project: First Algorithm Intercomparison Project. *Bull. Amer. Meteor. Soc.*, **75**, 401–419.
- Cressman, G. P., 1959: An operational objective analysis system. *Mon. Wea. Rev.*, **87**, 367–374.
- Dills, P. N., and S. B. Smith, 1992: Comparison of profiler and satellite cloud tracked winds. Preprints, *Sixth Conf. on Satellite Meteorology and Oceanography*, Atlanta, GA, Amer. Meteor. Soc., 155–158.
- Ferraro, R. R., 1997: SSM/I derived global rainfall estimates for climatological applications. *J. Geophys. Res.*, **102**, 16 715–16 735.
- , and Q. Li, 2002: Detailed analysis of the error associated with the rainfall retrieved by the NOAA/NESDIS/SSM/I algorithm: II. Rainfall over land. *J. Geophys. Res.*, **107**, 4680–4686.
- , F. Weng, N. C. Grody, and L. Zhao, 2000: Precipitation characteristics over land from the NOAA-15 AMSU sensor. *Geophys. Res. Lett.*, **27**, 2669–2672.
- Herman, L. D., 1992: Obtaining cloud motion vectors from polar orbiting satellites. Preprints, *Sixth Conf. on Satellite Meteorology and Oceanography*, Atlanta, GA, Amer. Meteor. Soc., 110–113.
- Higgins, R. W., W. Shi, E. Yarosh, and R. Joyce, cited 2000: Improved

- United States precipitation quality control system and analysis. [Available online at [http://www.cpc.ncep.noaa.gov/research-papers/ncep\\_cpc\\_atlas/7/index.html](http://www.cpc.ncep.noaa.gov/research-papers/ncep_cpc_atlas/7/index.html).]
- Hong, Y., C. Kummerow, and W. S. Olson, 1999: Separation of convective/stratiform precipitation using microwave brightness temperature. *J. Appl. Meteor.*, **38**, 1195–1213.
- Huffman, G. J., R. F. Adler, E. F. Stocker, D. T. Bolvin, and E. J. Nelkin, 2003: Analysis of TRMM 3-hourly multi-satellite precipitation estimates computed in both real and post-real time. Preprints, *12th Conf. on Satellite Meteorology and Oceanography*, Long Beach, CA, Amer. Meteor. Soc., CD-ROM, P4.11.
- Janowiak, J. E., R. J. Joyce, and Y. Yarosh, 2001: A real-time global half-hourly pixel-resolution IR dataset and its applications. *Bull. Amer. Meteor. Soc.*, **82**, 205–217.
- Ji, Y., and E. Stocker, 2003: Ground validation of TRMM and AMSU microwave precipitation estimates. Preprints, *Int. Geoscience and Remote Sensing Symp. 2003*, Toulouse, France, IEEE, CD-ROM, INT-B33.09.
- Joyce, R. J., J. E. Janowiak, and G. J. Huffman, 2001: Latitudinally and seasonally dependent zenith-angle corrections for geostationary satellite IR brightness temperatures. *J. Appl. Meteor.*, **40**, 689–703.
- Klazura, G. E., and D. A. Imy, 1993: A description of the initial set of analysis products available from the NEXRAD WSR-88D system. *Bull. Amer. Meteor. Soc.*, **74**, 1293–1312.
- Kummerow, C., W. S. Olson, and L. Giglio, 1996: A simplified scheme for obtaining precipitation and vertical hydrometeor profiles from passive microwave sensors. *IEEE Trans. Geosci. Remote Sens.*, **34**, 1213–1232.
- , and Coauthors, 2001: The evolution of the Goddard profiling algorithm (GPROF) for rainfall estimation from passive microwave sensors. *J. Appl. Meteor.*, **40**, 1801–1820.
- Lazzara, M. A., and Coauthors, 1999: The man computer interactive data access system: 25 years of interactive processing. *Bull. Amer. Meteor. Soc.*, **80**, 271–284.
- Li, Q., R. Ferraro, and N. C. Grody, 1998: Detailed analysis of the error associated with the rainfall retrieved by the NOAA/NESDIS SSM/I rainfall algorithm: Part I. Tropical oceanic rainfall. *J. Geophys. Res.*, **103**, 11 419–11 427.
- McCollum, J. R., W. F. Krajewski, R. R. Ferraro, and M. B. Ba, 2002: Evaluation of biases of satellite rainfall estimation algorithms over the continental United States. *J. Appl. Meteor.*, **41**, 1065–1080.
- Miller, S. W., P. A. Arkin, and R. J. Joyce, 2001: A combined microwave/infrared rain rate algorithm. *Int. J. Remote Sens.*, **22**, 3285–3307.
- Purdum, J. F. W., and P. N. Dills, 1994: Cloud motion and height measurements from multiple satellites including cloud heights and motions in polar regions. Preprints, *Seventh Conf. on Satellite Meteorology and Oceanography*, Monterey, CA, Amer. Meteor. Soc., 408–411.
- Shenk, W. E., and E. R. Kreins, 1970: A comparison between observed winds and cloud motions derived from satellite infrared measurements. *J. Appl. Meteor.*, **9**, 702–710.
- Simpson, J. R., R. F. Adler, and G. R. North, 1988: A proposed Tropical Rainfall Measuring Mission (TRMM) satellite. *Bull. Amer. Meteor. Soc.*, **69**, 278–295.
- Smith, E., and D. Phillips, 1972: Measurements from satellite platforms. Annual Satellite Rep. NASS-11542, SSEC, University of Wisconsin—Madison, 53 pp.
- Turk, F. J., E. E. Ebert, B.-J. Sohn, H.-J. Oh, V. Levizzani, E. A. Smith, and R. Ferraro, 2003: Validation of an operational global precipitation analysis at short time scales. Preprints, *12th Conf. on Satellite Meteorology and Oceanography*, Long Beach, CA, Amer. Meteor. Soc., CD-ROM, J1.2.
- Vincente, G. A., 1994: Hourly retrieval of precipitation rate from the combination of passive microwave and infrared satellite measurements. Ph.D. dissertation, University of Wisconsin—Madison, 127 pp.
- , J. C. Davenport, and R. Scofield, 1999: The role of orographic and parallax corrections on real time high resolution satellite rainfall estimation. Preprints, *The 1999 EUMETSAT Meteorological Satellite Data Users' Conf.*, Copenhagen, Denmark, EUMETSAT, 161–168.
- Weng, F. W., L. Zhao, R. Ferraro, G. Pre, X. Li, and N. C. Grody, 2003: Advanced Microwave Sounding Unit (AMSU) cloud and precipitation algorithms. *Radio Sci.*, **38**, 8068–8079.
- Weymouth, G., G. A. Mills, D. Jones, E. E. Ebert, and M. J. Manton, 1999: A continental-scale daily rainfall analysis system. *Aust. Meteor. Mag.*, **48**, 169–179.
- Wilks, D. S., 1995: *Statistical Methods in the Atmospheric Sciences: An Introduction*. Academic Press, 467 pp.
- Yang, G. Y., and J. Slingo, 2001: The diurnal cycle in the Tropics. *Mon. Wea. Rev.*, **129**, 784–801.
- Zhao, L., and F. Weng, 2002: Retrieval of ice cloud properties using the Advanced Microwave Sounding Unit (AMSU). *J. Appl. Meteor.*, **41**, 384–395.
- , —, and R. Ferraro, 2001: A physically-based algorithm to derive surface rainfall using Advanced Microwave Sounding Unit-B (AMSU-B) measurements. Preprints, *11th Conf. on Satellite Meteorology and Oceanography*, Madison, WI, Amer. Meteor. Soc., 371–374.